

Thermal and Visual Tracking of Photovoltaic Plants for Autonomous UAV Inspection

Luca Morando, Carmine Tommaso Recchiuto, Jacopo Callà, Paolo Scuteri and Antonio Sgorbissa

Abstract—Since photovoltaic (PV) plants require periodic maintenance, using Unmanned Aerial Vehicles (UAV) for inspections can help reduce costs. The thermal and visual inspection of PV installations is currently based on UAV photogrammetry. A UAV equipped with a Global Positioning System (GPS) receiver is assigned a flight zone: the UAV will cover it back and forth to collect images to be later composed in an orthomosaic. The UAV typically flies at a height above the ground that is appropriate to ensure that images overlap even in the presence of GPS positioning errors. However, this approach has two limitations. Firstly, it requires to cover the whole flight zone, including “empty” areas between PV module rows. Secondly, flying high above the ground limits the resolution of the images to be later inspected. The article proposes a novel approach using an autonomous UAV equipped with an RGB and a thermal camera for PV module tracking. The UAV moves along PV module rows at a lower height than usual and inspects them back and forth in a boustrophedon way by ignoring “empty” areas with no PV modules. Experimental tests performed in simulation and an actual PV plant are reported.

Index Terms—Aerial Systems, Autonomous Vehicle Navigation, Photovoltaic (PV) plant inspection

I. INTRODUCTION

WE are currently facing a worldwide energy challenge that requires us to search for alternatives to fossil fuels, including green and renewable energies [1]. According to [2], in 2019, renewable energy sources made up 34% of gross electricity consumption in the EU-27, slightly up from 32% in 2018. While wind and hydropower accounted for two-thirds of the total electricity generated from renewable sources (35% each), the remaining one-third of the electricity generated was from solar power (13%), solid biofuels (8%), and other renewable sources (9%). The analysis also shows how solar power is the renewable source experiencing the fastest growth, given that in 2008 it accounted for around 1%.

Solar energy plants offer many advantages since they have a long life, are environmentally friendly, noise-free, and clean. However, photovoltaic (PV) installations need periodic maintenance since they always need optimal conditions to work properly [3]. Surface defects [4], [5], [6], [7], [8] are the most common problems. They can be detected through human inspection: a qualified operator can easily detect different defects, including snail trails¹, yellowing of the encapsulant, delamination and bubble formation in the encapsulant, front surface soiling, busbar oxidation, or impact from physical objects. However, a human inspection might be time-consuming

if the PV plant is very large (or in particular conditions, e.g., panels are mounted on a rooftop). In order to reduce the cost and time required for maintenance, methods exist [9] to estimate the presence and impact of global defects through the analysis of the power output. However, this approach presents two main disadvantages: a reference power production is required, and the exact locations of defects cannot be identified.

Unmanned Aerial Vehicles (UAVs) have been recently proposed for PV inspections. In the past decades, research made significant steps forward concerning the development of UAVs for monitoring applications, including the inspection of power transmission lines [10], gas and oil pipelines [11], precision agriculture [12], and bridges [13]. Indeed, the ability of multirotor UAVs to hover and move freely in the air and the fact that they can be easily piloted and equipped with different sensors make this technology very appealing in monitoring scenarios. Generally, UAVs used for PV inspection are equipped with a thermal camera (which may or may not complement a standard RGB camera or other sensors) to identify defects that can produce heat anomalies on the solar panels.

The use of UAVs reduces the inspection time but, on the other hand, creates a larger amount of raw data to be processed, which must meet some requirements in terms of resolution and position accuracy. Currently, the inspection of PV plants through thermovisual imagery is mostly based on UAV photogrammetry [14], [15], [16]. A UAV equipped with a Global Positioning System (GPS) receiver and an Inertial Measurement Unit (IMU) is assigned a flight zone: it will cover this area back and forth by ensuring the required overlapping of images, horizontally and vertically, to be later composed in an orthomosaic. The UAV typically flies at a height above the ground that is appropriate to ensure that the images overlap even in the presence of GPS positioning errors. However, this approach has two limitations. Firstly, it requires covering the whole zone including “empty” areas between PV module rows: depending on how PV module rows have been arranged in the PV plant, there may be large areas without PV panels to be inspected. Secondly, flying high above the ground limits the impact of positioning errors, which is good, but also the resolution of the images to be later inspected.

One could imagine a solution not based on photogrammetry: the UAV could be instructed to move along PV module rows by inspecting them in a “boustrophedon” way (i.e., back and forth like the ox turns while plowing, Figure 1) at a lower height so that the panel almost completely occupies the camera’s field of view and ignoring the areas where there are no PV modules to be inspected, thus ensuring

L. Morando, C. Recchiuto, A. Sgorbissa are with University of Genova; J. Calla and P. Scuteri are with JPDroni S.r.l. // Contact author email: antonio.sgorbissa@unige.it

¹A snail trail is a discoloration of the panel.

higher resolution images and fewer data to be processed. To implement this mechanism, it might seem sufficient to provide a sequence of waypoint coordinates to the UAV's mission planner before take-off. The waypoints might, in their turn, be chosen during the pre-flight setup, with an operator drawing the desired path on Google Earth images showing the solar plant to be inspected. However, as discussed in [9], the error in planimetric coordinates of the objects captured in Google Earth ranges from 5 to 10 meters. This aspect, together with the intrinsic inaccuracy of the GPS signal, will likely produce a wrong UAV placement, determine a wrong alignment of the UAV with the PV module rows, increase the amount of useless data acquired, and reduce performances.

Based on these premises, a different solution using sensor information to correct in real-time the error between the UAV and the actual position of PV modules is needed. The main contribution of this article is a portfolio of techniques for PV module segmentation and UAV navigation through visual servoing based on the onboard RGB and thermal cameras. Please remark that, in PV plant inspection, a thermal camera is required for detecting defects: then, using both RGB and thermal cameras for PV module row tracking is particularly convenient as it may improve reliability in critical light or temperature conditions [9]. JP Droni² confirms that GPS-based photogrammetry is the only approach currently adopted in Italy (and, to the best of their knowledge, in the world) for PV inspection: in commercial applications, the UAV typically flies at 30-40 meters above the ground. The availability of visual servoing techniques based on PV module segmentation might produce a breakthrough by allowing UAVs to fly at a lower height to collect fewer, higher resolution images.

Figure 1 shows how the system works and introduces the main concepts used in the rest of the article.

- *PV midline*, a straight line in the middle of the PV module row that determines the desired motion direction.
- *PV end*, a point on the PV midline that identifies the end of the PV module row.
- *PV start*, a point that identifies the start of the new PV module row, whose position is computed with respect to the end of the previous row.

The upper left corner of Figure 1 shows a UAV moving along the PV rows in a boustrophedon way. The UAV moves from *PV start* to *PV end* along a *PV midline*. Then, it “jumps” to the next PV row and it starts moving again from the following *PV start* to its corresponding *PV end*, and so on.

The article is organized as follows. Section II surveys the relevant literature. Section III describes the system architecture. Section IV introduces the techniques used for PV module segmentation using RGB and thermal images. Section V introduces strategies for UAV autonomous navigation. Section VI presents the experimental results in a photorealistic simulated environment and a real PV plant. Finally, in Section VII, conclusions and directives for future research are given.

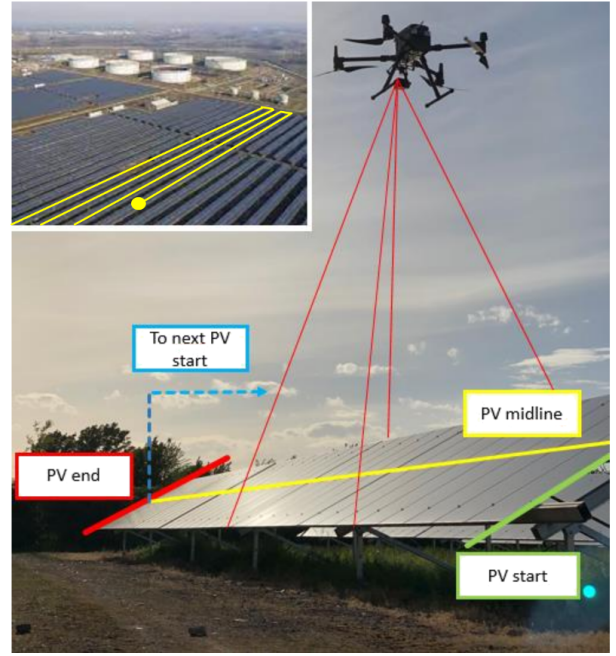


Fig. 1. System at work in a PV plant. The DJI Matrice 300 drone is equipped with a hybrid RGB and a thermal camera, the DJI Zenmuse XT2.

II. STATE OF THE ART

Various techniques and applications have been proposed for automatic defect detection from aerial images. For example, the authors of [17] and [18] use computer vision and machine learning techniques to detect and classify cracks and potholes in roads and highways using images taken by UAVs. Similarly, [19] and [20] address the inspection of power lines with UAVs, using techniques such as Faster region-based convolutional neural network (Faster R-CNN) [21] to detect defects and the Hough Transform [22] for cable detection. Strategies for automatic defect detection have also been applied to the PV plant scenario. For example, [23] proposes two different techniques for inspection and mapping, aerial IR/visual image triangulation and terrestrial IR/visual image georeferencing: the authors discuss the potential of both approaches in localizing defective PV modules. In [24], a Convolutional neural network (CNN) is used for defect recognition based on aerial images obtained from UAVs. The authors of [25] present an approach that unifies two region-based CNNs (R-CNN) to generate a robust detection approach combining thermography and telemetry data for panel condition monitoring. A model-based approach for the detection of panels is proposed in [26]: this work relies on the structural regularity of the PV arrays and introduces a novel technique for local hot spot detection from thermal images, based on a fast and effective algorithm for finding local maxima in the PV panel regions. In [27] a fully automated approach for detecting, classifying, and georeferencing thermal defects in the PV modules is proposed, which exploits a novel method based on image reprojection and function minimization to detect the panels from the images. These and similar works address only the problem of autonomous defect detection and georeferencing without using the acquired images as feedback for the UAV

²JP Droni Srl is a company in Genova providing aerial services for video productions, precision agriculture, and technical inspection of power plants.

to move autonomously along the inspection path.

The autonomous inspection of PV plants through UAV photogrammetry has been explored in the literature [14], [15], [28], [29]. The UAV is given a set of waypoints, usually arranged in such a way to cover a delimited area to ensure the required horizontal and vertical overlapping of images. Then, the UAV moves along the planned sequence of waypoints using GNSS/GPS data only, possibly negatively impacting data quality due to positioning errors [30]. An approach to generating an optimal waypoint path based on satellite images is proposed in [31] to reduce the error due to the misalignment of georeferenced images and the actual inspection site. The PV plant's boundary is extracted via computer vision techniques, and the system can re-compute the path if the UAV requires reaching a specific location (e.g., a PV module where a defect has been detected) or if the UAV cannot complete the initial path for any reason. In [32], a novel technique for boundary extraction is proposed using a Mask R-CNN architecture with a modified VGG16 backbone. The network is trained on the AMIR dataset [33]: an aerial imagery collection of PV plants from different countries. The work proposed in [16] uses a VGG16 CNN fed with images that underwent a Structure from Motion – MultiView Stereo (SfM-MVS) photogrammetric processing workflow to generate thermal orthomosaics of the inspected sites. These and similar approaches focus on planning a waypoint path with the objective to cover the whole area according to the principles of photogrammetry, i.e., they do not consider tracking individual PV module rows at a lower height from the ground to produce fewer and higher resolution images to be processed.

Visual Servoing is widely used in robotics. Many examples of UAV autonomous navigation based on data acquired through cameras exist in the literature, some involving inspection tasks. For example, an algorithm for detecting vertical features from images has been used in [34] to guide a UAV along a semi-linear path while flying over a highway in the US. This approach is based on the consideration that vertical edges are a characterizing attribute of highways that can be easily detected using methods such as RANSAC [35], which can also be used to predict splines [36] where sharp curves may occur. Similar techniques may be found in [37] and [38], where the authors respectively contributed to the field of precision agriculture and building inspection. In [37], a novel control technique based on a passivity-based visual servoing controller with dynamics compensation to track crops is described. The proposed system allows a UAV to move along straight lines such as those formed by structured crops. In [38], a complete navigation and inspection task is executed by an autonomous quadrotor. The most interesting part of this work is the approach used for road detection and navigation, which segments the image into predominant color layers before feeding it to DeepLabv3+ [39], a network trained for semantic segmentation. The road is then identified in the image and finally followed by the UAV by defining a sequence of control points.

Visual servoing was rarely applied to UAV navigation over large PV plants. This may also be due to the complexity of the scenario, which may have different characteristics in

terms of the number of PV module rows, their dimension, and mutual arrangement. Nevertheless, some attempts in this direction have been made in recent years. For example, in [40], the authors propose a vision-based guidance law to track PV module rows based on PV modules' edge detection. The approach extracts vertical edges from RGB images using a Hough Transform. Then, the detected misalignment between the PV row observed from images and the actual UAV position is fed to the navigation control law. Unfortunately, this approach has only been tested in simulation. An edge detection technique is also proposed in [41], where the metallic profile of the PV array is detected and segmented by combining color and feature extraction, using the Hough Transform and a Hue-Saturation-Value (HSV) model. Once the panels have been segmented, the velocity orthogonal to the PV module row is controlled to keep the UAV aligned. Both approaches rely on the tuning of parameters for edge extraction: notwithstanding this limitation, it is worth noticing that, in the "era of Deep Learning," many of the approaches mentioned above [37], [38], [40], [41] rely on model-based vision techniques for feature segmentation. In structured environments whose model is a priori known, such as PV plants, a model-based formulation of the problem may offer advantages in predictable and explainable behaviour [42] and possibly robustness to adversarial attacks [43] that cannot be ignored. As an aside, this is also confirmed by AI in aviation (particularly Machine Learning) still being at the beginning. Even if AI is widespread in subdomains like logistics and fuel consumption estimation [44], [45], AI techniques in flight control can hardly be found in real-world application scenarios.

III. SYSTEM ARCHITECTURE

The system can autonomously perform UAV-based PV inspection centered on the following core elements.

- A procedure for detecting PV modules in real-time using a thermal or an RGB camera (or both).
- A procedure for correcting errors in the relative position of the *PV midline*, initially estimated through GPS, by merging thermal and RGB data.
- A navigation system provided with a sequence of georeferenced waypoints defining an inspection path over the PV plant, which uses the estimated position of the *PV midline* for making the UAV move along the path with bounded navigation errors.

The software architecture implemented in ROS [46] is shown in Figure 2. ROS nodes (1) and (2) acquire and process raw frames from the RGB and the thermal camera and perform PV module segmentation, Sections IV-A, IV-B. As an output of this process, each node returns the parameters, in the image frame, of the straight lines running in the middle of the detected PV module rows. To increase segmentation accuracy with varying environmental conditions, node (3) implements an optimization procedure to find the best parameters for segmentation: some details about this procedure are in Sections IV-C. Node (4) merges subsequent observations, independently performed by the two cameras in subsequent time instants. Since the parameters of straight lines independently extracted

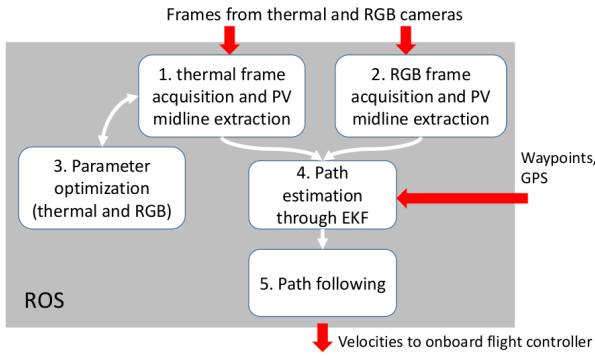


Fig. 2. System architecture implemented in ROS.

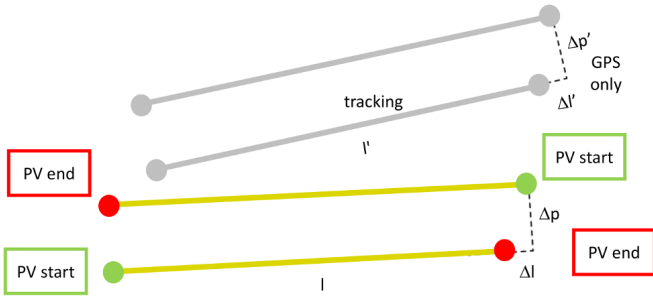


Fig. 3. A priori computed waypoints (colored circles) and PV module row's position observed during the mission (gray part).

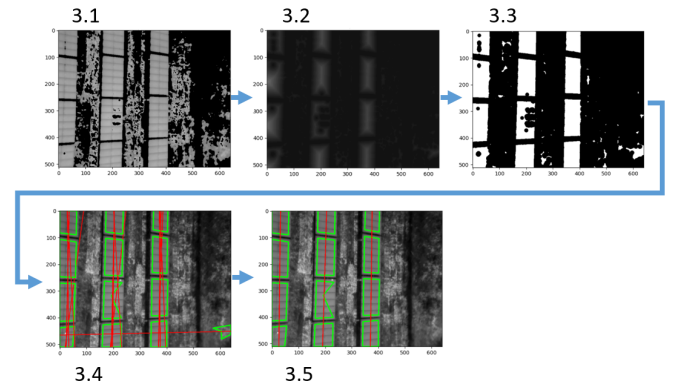
by (1) and (2) may be affected by errors, an Extended Kalman Filter (EKF) is used to estimate the *PV midline* by merging the observations provided in real-time by nodes (1) and (2) with a priori knowledge, Sections V-A and V-B. Finally, node (5) uses the estimated reference path for controlling the UAV along its path through visual servoing, Section V-C.

PV module row tracking is not sufficient: node (5) also needs rules to instruct the UAV to move to the next row when the previous one has been completed. This means we need a waypoint-based reference path defining the order according to which *PV module rows* shall be inspected. Remember that waypoints can be labelled as *PV start* or *PV end* and are acquired before the inspection through Google Earth or other georeferenced images (possibly affected by positioning errors), Figure 1. They shall be connected in a sequence such that

- the path goes from a *PV start* to a *PV end* waypoint when moving along a *PV row*: in this case, the distance between *PV start* and *PV end* defines how far a *PV midline* shall be followed before moving to the next one;
- the path goes from a *PV end* to a *PV start* waypoint when jumping to the next *PV row*: in this case, the position of *PV start* relative to *PV end* defines the start of the new row with respect to the previous one.

Currently, waypoints are manually chosen, but this process might be automated starting from a georeferenced image of the whole plant.

As already discussed, real-time segmentation and visual tracking of *PV module rows* may play a key role in successful navigation. Indeed, waypoint-based navigation relying on the embedded positioning system of the UAV (typically merging

Fig. 4. Pipeline for *PV module* detection from thermal images: 1) thresholded image; 2) distance matrix; 3) binarized image; 4) segmentation and regression line extraction; 5) clustering and *PV midline* estimation.

GPS, IMUs, and compass) has well-known limitations: the absolute position of *PV start* and *PV end* waypoints, as well as GPS data, may be affected by large errors in the world frame. On the opposite, by using visual servoing to move along a *PV row*, we only need to ensure that the relative position of adjacent waypoints and the small UAV displacement from a *PV module row* to the next one performed with GPS only are sufficiently accurate. Figure 3 shows this concept: the colored part of the Figure represents a priori computed waypoints; the gray part represents the observed position of *PV module rows* while tracking them. The proposed solution works even when the absolute error between the a priori computed and the observed position of *PV module rows* is huge, given that $\Delta l \approx \Delta l'$ and $\Delta p \approx \Delta p'$ (the additional requirement $l \approx l'$ holds if one uses GPS to measure the length of the *PV module row* instead of implementing some sort of “end-of-row detector”). These assumptions look reasonable since georeferenced waypoints computed from Google Earth images and GPS data may be affected by large biases (which, in the case of GPS, vary with time) but tend to be locally coherent – i.e., the relative error of waypoints (respectively, GPS-data) with respect to previous waypoints (respectively, GPS-data acquired in nearby locations) is small.

Eventually, even if it is not the focus of this article, remark that additional high-resolution thermal images (not used for navigation) are captured and stored in the onboard storage of the UAV for defect detection (possibly performed after the UAV has ended the mission). In this case, the UAV's flying height and speed determine the frequency of acquisition to guarantee that images are overlapping.

IV. DETECTION OF PV MODULES

A. Segmentation of *PV modules* via thermal camera

Each image captured by the thermal camera can be represented as a matrix. The image frame I is in the upper left corner of the image plane and $i(u, v)$ is a function that associates a thermal value to each pixel (u, v) : thermal cameras return the thermographic image as a mono-channel grayscale intensity matrix, where the pixels intensities may assume values between 0 and 255.

As a first step, a mask F is applied to the image after choosing two thresholds th_1 and th_2 . That is, each image pixel is processed as follows:

$$f(u, v) = \begin{cases} i(u, v), & \text{if } th_1 < i(u, v) < th_2 \\ 0, & \text{otherwise.} \end{cases} \quad (1)$$

While the values of th_1 and th_2 may be a priori chosen based on the analysis of previously acquired images³, there may be the need to fine-tune them when environmental conditions change. Please, refer to Section IV-C about the strategy used for this purpose. As expected and visible in Figure 4.1, the application of this mask is not sufficient to make the PV modules emerge unambiguously: in some regions, the ground may have the same temperature as the panels.

As a second step, we filter out the noise by exploiting a priori domain knowledge: even if pixels with thermal intensity in the selected range can also be found outside PV panels, the panels are characterized by a higher density of pixels falling within the thresholds. Then, the entire image is filtered by computing a distance matrix D storing the Euclidean distance of each pixel in F from the closest pixel whose value is zero. That is, for each pixel (u, v) , we compute:

$$d(u, v) = \sqrt{(u_{zero} - u)^2 + (v_{zero} - v)^2} \quad (2)$$

where u_{zero} and v_{zero} are, respectively, the row and the column of the zero value pixel nearest to (u, v) , Figure 4.2.

As a third step, each pixel of the distance matrix D is transformed into a binary intensity value as follows:

$$b(u, v) = \begin{cases} 1, & \text{if } d(u, v) > th_3 \\ 0, & \text{otherwise} \end{cases} \quad (3)$$

where th_3 can be interpreted as a distance threshold to determine whether a pixel (u, v) in the original image belongs to a high-density region, Figure 4.3. As for th_1 and th_2 , the threshold th_3 is set a priori and then fine-tuned with the optimization procedure described in Section IV-C. Groups of neighbouring pixels are clustered into N polygonal regions S_i : during the process, only the regions larger than a given number of pixels survive, whereas smaller clusters are deleted⁴.

As a fourth step, we compute, for each segmented region S_i , a regression line through polynomial curve fitting⁵: starting from regions S_i , N regression lines are computed, each described by a point $p_i = (u_i, v_i)$ and a unitary vector l_i defining a direction in the image plane I , Figure 4.4.

As a fifth step, the detection algorithm requires clustering all regions S_i that are likely to correspond to PV modules aligned in the same row, by using their corresponding regression lines. That is, starting from a subset of individual shapes S_i and the corresponding regression lines, a unique cluster C_j (more robust to noise) is computed with $j = 1, \dots, J$. Specifically, two regions S_i and S_k are clustered in C_j if the corresponding regression lines meet the two conditions below:

- The magnitude of the difference vector should be smaller than a threshold $\|l_i - l_k\| < th_A$, i.e., the two lines tend to be parallel.
- The average point-line distance between all pixels in the image plane belonging to the first line and the second line should be below a threshold $dist(p_i, l_i, p_k, l_k) < th_B$, i.e., the two lines tend to be close to each other.

Parameters th_A and th_B depend on a priori geometrical consideration and not on environmental conditions; therefore they are not subject to optimization. Clustering is iteratively repeated for all shapes S_i : then, a new regression line is computed for each cluster C_j , Figure 4.5. The final output of the process is a set of J lines, each possibly corresponding to multiple PV modules belonging to the same row. Each observed *PV midline* is represented in the image frame through a couple of points $o_j = (p'_j, p''_j)$, with $p'_j = (u'_j, v'_j)$, $p''_j = (u''_j, v''_j)$ corresponding to the intersection of the line with the borders of the image.

B. Segmentation of PV modules via RGB camera

The algorithm developed to process thermal images is almost completely reused for RGB images, except for the initial steps required for PV module segmentations, Figures 5.1 and 5.2.

When using RGB images, the rows of PV modules can be detected thanks to their color in contrast with the background. Then, as a first step, the original image I is transformed into the hue-saturation-value (HSV) color space: Figure 5.1 shows the result, RGB-rendered by using H values for the R channel, S for G, and V for B. As a second step, the PV modules are segmented from the background by thresholding the image in all the three HSV channels, Figure 5.2. The lower HSV thresholds th_4, th_5, th_6 and the higher HSV thresholds th_7, th_8, th_9 are manually chosen based on a priori domain knowledge and then fine-tuned before operations, as explained in Section IV-C.

The result is a binary image defined as follows:

$$b(u, v) = \begin{cases} 1, & \text{if } th_4 < H(u, v) < th_7 \\ & \wedge th_5 < S(u, v) < th_8 \\ & \wedge th_6 < V(u, v) < th_9 \\ 0, & \text{otherwise} \end{cases} \quad (4)$$

Please remember that, in the HSV color space, hue is measured in degrees from 0 to 360 and is periodic⁶: red takes negative and positive values around zero, which means that the first condition in (4) must be changed to “if not($th_4 \leq H(u, v) \leq th_7$)” in case we need to segment areas characterized by a reddish color.

The final steps of the process, as for thermal images, require to segment polynomial regions S_i, \dots, S_N in $b(u, v)$, each associated with a regression line, that are finally clustered into J clusters C_j , each corresponding to an observed line $o_j = (p'_j, p''_j)$, Figures 5.3 and 5.4.

³During our experiments, we acquired a dataset of images of a PV plant through a DJI Zenmuse H20T camera, composed of $430\ 640 \times 512$ thermal images.

⁴OpenCv function `findContours`.

⁵OpenCv function `fitLine`.

⁶In OpenCV, hue is encoded in a byte and ranges from 0 to 179.



Fig. 5. Pipeline for PV module detection from RGB images: 1) Transformation into HSV space; 2) binarized image; 3,4) segmentation, regression line extraction and clustering, PV midlines estimation.

C. Thresholds tuning

PV module detection needs appropriate thresholding. For thermal images, we must choose the lower and upper bounds th_1 and th_2 of thermal intensity in (1) and the distance threshold th_3 in (3); for RGB images, we need to choose the minimum th_4, th_5, th_6 and the maximum th_7, th_8, th_9 values for each HSV channel in (4). Thresholds are chosen using a procedure that maximizes the number of PV modules detected in thermal and RGB images separately taken as well as the matches between the PV modules detected in both images. The following assumes that thermal and RGB images are overlapping, which can be ensured through rototranslation and scaling if needed. Under this constraint, despite the segmented PV module shapes may be slightly different depending on the acquisition method used⁷, they are expected to roughly occupy the same regions in pairwise images.

The algorithm used to minimize the cost function is L-BFGS-B [47], a limited-memory algorithm that can be used to minimize a non-linear cost function subject to simple bounds on the variables. The algorithm is particularly appropriate to solve large non-linear, non-convex optimization problems in which the Hessian is hard to compute.

We assume that the UAV reaches the start position of the first PV module, possibly remotely controlled by a human operator, with its front oriented towards the direction of the PV modules row. Then, the following non-linear, non-convex optimization problem on variables $th_i, i = 1 \dots 9$, is solved:

$$\min_{th_1-th_9} - \sum_{i=1}^{N_T} (c_{i,T} + r_{i,TR}) - \sum_{i=1}^{N_R} (c_{i,R} + r_{i,RT}) \quad (5)$$

where (5) is the cost function, whose value expresses the “quality” of the segmentation algorithm given a set of thresholds $th_1 - th_9$ subject to disequality constraints.

Mathematical details of the cost are not discussed for the sake of brevity. Intuitively, please remember that the thermal camera computes a set of N_T segmented regions $S_i, i = 1 \dots N_T$, and the RGB camera computes a set of N_R segmented regions $S_i, i = 1 \dots N_R$. Then the first sum in the cost function refers to regions extracted from the thermal camera, and the second sum refers to regions extracted from the RGB camera. For each region S_i extracted from thermal images, the cost function comprises two terms $c_{i,T}$

⁷In thermal images, the temperature of the junctions between adjacent PV panels may be different from PV panels themselves, resulting in a sequence of smaller rectangular shapes. In RGB images, this never happens, returning larger rectangular areas composed of multiple panels.

and $r_{i,TR}$. The term $c_{i,T}$ intuitively considers how close S_i is to a rectangular shape oriented along the current direction of motion, and how close S_i 's extension is to a value that depends on the PV module geometry and the UAV height from the ground. The term $r_{i,TR}$ measures the pixel-wise correlation between the region S_i and the binary mask extracted from the paired RGB image covering the same area: $r_{i,TR}$ is higher if the region S_i segmented from the thermal image is also present in the RGB image. The two terms $c_{i,R}$ and $r_{i,RT}$ are computed similarly, starting from regions extracted from RGB images.

Please notice that jointly optimizing all variables might be time-consuming: for this reason, during experiments in PV plants, we decompose the problem (5) into two sub-problems. Firstly, we only consider RGB images and search for the minimum of $-\sum_{i=1}^{N_R} c_{i,R}$: that is, we ignore correlation with thermal images. Secondly, we consider thermal images only and search for the minimum of $-\sum_{i=1}^{N_T} (c_{i,T} + r_{i,TR})$. This simplification seems a good compromise to reduce computation time if we want to repeat the procedure, e.g., at the PV start of each new row.

V. UAV NAVIGATION

A. From the image frame F to the camera frame C

To describe the motion of the UAV body in the world frame, we define a mobile camera frame C with origin in the center of the camera lens, xy -plane parallel to the uv -image plane at distance f (focal length), x -axis pointing to the UAV front, and z -axis downward⁸. The origin of the camera frame moves as the drone moves along the PV module row: since the UAV is endowed with a gimbal mechanism that keeps the xy -plane of the camera frame parallel to the XY -plane of the world frame, all the transformations involving the image, world, or camera frame are simpler since the camera is always looking perpendicularly to the ground in a nadiral position.

Given a point $p_i = (u_i, v_i)$ in the image frame, its position (x_i^C, y_i^C) in the camera frame C can be computed as:

$$x_i^C = -\frac{k}{f}(v_i - \frac{V}{2})z_g^C \quad (6)$$

$$y_i^C = \frac{k}{f}(u_i - \frac{U}{2})z_g^C \quad (7)$$

where k converts the pixel size in meters and z_g^C is the distance of the ground from the origin of the camera frame. The thermal and RGB cameras are typically mounted on the same rigid body a few centimeters apart in commercial products. Then, if we set C 's origin in the thermal camera lens, all observations done in the RGB image frame shall ideally undergo a transformation to map them in C . This is not mentioned in the following for brevity's sake.

Using the formula above, for every observed line $p'_j = (u'_j, v'_j), p''_j = (u''_j, v''_j)$ in the image frame returned by the procedure in Section IV (either by the thermal or RGB camera), we compute the parameters $o^C = (a^C, b^C)$ of an observed line $y^C = a^C x^C + b^C = 0$ in the camera frame C through simple

⁸That is x heads towards $-v$ in the image plane, and y heads towards u .

geometrical considerations. Please notice that we can ignore the z^C coordinate since the xy plane of the camera frame is parallel to the ground thanks to gimbal stabilization: the UAV altitude will be separately controlled through an independent mechanism. Then, the equation $y^C = a^C x^C + b^C = 0$ should be better interpreted as the equation of a plane perpendicular to the xy plane of the camera frame.

B. Path estimation through EKF

The observations $o^C = (a_j^C, b_j^C)$, where $j = T, R$ correspond, respectively, to the thermal and RGB cameras, are iteratively merged to estimate the *PV midline* parameters in the world frame, described as a straight line with implicit equation $y^W = a^W x^W + b^W$ (once again, this should be better interpreted as a plane perpendicular to the ground).

For this purpose, an Extended Kalman Filter [48] is used. The state $m^W = (a^W, b^W)$ of the *PV midline* is described in the world frame W in order to keep the system dynamics constant: in this case, the state m^W to be estimated does not change as the UAV moves along the PV module row since the latter is not moving. However, the observations $o^C = (a_j^C, b_j^C)$ acquired through cameras are expressed in the camera frame; therefore the system needs to know the UAV pose in order to map them on the world frame through the EKF observation matrix H . In this work, we assume that the pose x^W, y^W and yaw θ^W of the camera frame in the world frame is computed by the low-level flight controller embedded in the UAV, which typically merges GPS, IMUs, and compass. Once again, thanks to the gimbal mechanism and the fact that we control the altitude through an independent mechanism, z^w is ignored since the pitch and roll of the camera can be approximated to be zero. Using the embedded UAV positioning system may be counter-intuitive, since we repeatedly stated that it is affected by absolute errors. However, similar to what happens in the passage from one PV module row to the next one (Figure 3), it is deemed appropriate since we are not interested in knowing the absolute UAV pose with high accuracy. It is sufficient that the pose error slowly changes in time and that it is almost constant along one PV module row (which typically happens with GPS low-frequency errors) to guarantee that subsequent observations are coherent with each other when mapped to the world frame without producing abrupt changes in the state estimate⁹.

The EKF allows for merging observations acquired at different times originating from the thermal and RGB camera. In the following, we use the notation $\hat{m}_{k+1|k}^W = \hat{m}_k^W$ to describe the evolution of the state at the prediction step $k+1$ due to control inputs (which, as already mentioned, is constant), and the notation $o_{k+1}^C = (a_j^C, b_j^C)$ to describe the observation made at the update step $k+1$ by the j^{th} sensor.

During the update step, we need a measurement model $\hat{o}_{k+1}^W = H_{k+1} \hat{m}_{k+1|k}^W$, where H_{k+1} is the Jacobian of the non-linear observability function $h(m)$, which allows for obtaining the expected measurement \hat{o}_{k+1}^C from the estimated

state $\hat{m}_{k+1|k}^W$ given the current camera position and yaw x^W, y^W, θ^W . Specifically, $h(m^W)$ has two components:

$$\begin{aligned} h_1(m^W) &= \frac{a^W - \tan \theta^W}{1 + a^W \tan \theta^W} \\ h_2(m^W) &= \frac{x^W a^W + b^W - y^W}{\cos \theta + \sin \theta a^W} \end{aligned} \quad (8)$$

whose Jacobian with respect to (a^W, b^W) needs to be evaluated in $\hat{a}^W, \hat{b}^W, x^W, y^W$ and θ^W .

The EKF is a recursive algorithm consisting in two steps referred to as state prediction and update. The prediction at step $k+1$ can be expressed as:

$$\hat{m}_{k+1|k}^W = A \hat{m}_{k|k}^W + B u_{k|k}, \quad (9)$$

where A , in our case, is the identity matrix and $B = 0$ since the state m^W is invariant over time when expressed in world coordinates. The state equations are linear, and the EKF is needed only because of the non-linearity of the observation model. The error covariance matrix is

$$P_{k+1|k} = A P_{k|k} A^T + Q, \quad (10)$$

where the process noise $Q \approx 0$. Since the state is not evolving, Q should be null: still, we empirically add a very small contribution to the error covariance matrix to ensure that new observations will keep on contributing to the state estimate.

Only the observations o_{k+1}^W that are ‘‘sufficiently close’’ to the estimated state (in the same spirit adopted for clustering in Section IV) are considered during the update step. In contrast, outliers are rejected to avoid undesired corrections due to the detection of neighbouring PV rows running in parallel to the tracked one. Finally, in the correction step, the Kalman gain is computed starting from the covariance of the measurement noise R and P as usual:

$$K_{k+1} = P_{k+1|k} H_{k+1}^T (H_{k+1} P_{k+1|k} H_{k+1}^T + R_j)^{-1}. \quad (11)$$

The a posteriori estimate is updated as:

$$\hat{m}_{k+1|k+1}^W = \hat{m}_{k+1|k}^W + K_{k+1} (o_{k+1} - H_{k+1} \hat{m}_{k+1|k}^W), \quad (12)$$

$$P_{k+1|k+1} = (I - K_{k+1} H_{k+1}) P_{k+1|k}. \quad (13)$$

The covariance matrix R_j relative to each sensor $j = T, R$ is evaluated experimentally and takes into account both segmentation errors due to the procedure in Section IV and the fact that, during an inspection, the GPS error may be subject to minor variations, therefore partially conflicting with the assumption of a constant GPS error in (8).

The EKF is initialized with $\hat{m}_{0|0}^W = (a^W, b^W)$ estimated at step $k=0$ by considering the two waypoints *PV start* and *PV end* of the initial PV module row. Even if the state may be affected by a significant error, it will be iteratively reduced by the EKF through subsequent observations as the UAV moves.

C. Path following

Path following works in two different phases: (i) when the UAV is moving from *PV start* to *PV end* along a PV module row; (ii) when it is moving from *PV end* of the current row to *PV start* of the next one (Figure 3).

⁹Ideally, we could attempt to estimate the UAV pose in the world frame by merging the sensors above with the observations made with cameras, by hypothesizing an augmented state vector including both the PV midline and the UAV pose [49]. However, this possibility is not explored in this work.

In phase (i), navigation is based on *PV midline* tracking. After each iteration of the EKF, the estimated parameters describing the *PV midline* in the world frame $\hat{m}_{k+1|k+1}^W = (\hat{a}^W, \hat{b}^W)$ are mapped back onto the camera frame for path following, yielding (a_{ref}^C, b_{ref}^C) . Then, given the equation $y^C = a_{ref}^C x^C + b_{ref}^C$ in the camera frame, the distance error

$$e = -b_{ref}^C / (a_{ref}^{C2} + 1)^{1/2} \quad (14)$$

is computed, as well as the parallel and the perpendicular vectors to the path

$$V_{\parallel}^C = (1/a_{ref}^C, 1), \quad V_{\perp}^C = (-1, 1/a_{ref}^C). \quad (15)$$

Given the quantities above, different approaches can be used to control the distance from the *PV midline*. In this work, we adopt a simple “carrot chasing” approach [50]: the parallel and perpendicular vectors are added to compute the position of a virtual moving target using the distance error e as a weighting factor for V_{\perp}^C , and a PID controller is used to tune the UAV velocities to regulate the distance from the target to zero.

In phase (ii), the UAV uses the pose information x^W, y^W, θ^W returned by the onboard flight controller (merging GPS, IMU, and compass) to move from *PV end* to the next *PV start*.

In both phases, the altitude is separately controlled using embedded sensors returning the height from the ground¹⁰.

VI. EXPERIMENTS

This Section presents the experiments conducted in a real PV plant and a realistic simulation environment.

A. Material and Methods

Real-world experiments in a PV plant were conducted using a DJI Matrice 300 aircraft equipped with a DJI Zenmuse XT2 camera. The camera has a field of view of 57.12×42.44 degrees and a gimbal mechanism. An onboard DJI Manifold PC equipped with an NVIDIA Jetson TX2 and 128GB of internal memory performs all the computations described in previous Sections to process the acquired images and control the UAV.

The simulation environment deserves more attention. In addition to the onboard DJI Manifold performing the core computations, two programs were running in parallel to simulate, respectively, the dynamics and the perception of the UAV:

- The DJI Matrice Simulator, embedded in the DJI Matrice 300. When the DJI Manifold is connected to the drone and the OSDK is enabled, this program simulates the UAV dynamics based on the commands received from the ROS nodes executed on the DJI Manifold.
- The Gazebo Simulator, running on an external Dell XPS notebook with an Intel i7 processor and 16 GB of RAM, integrated with ROS. Here, only the thermal and RGB camera and the related gimbal mechanism were simulated to provide the DJI Manifold with images acquired in the simulated PV plant. The cameras’ position inside

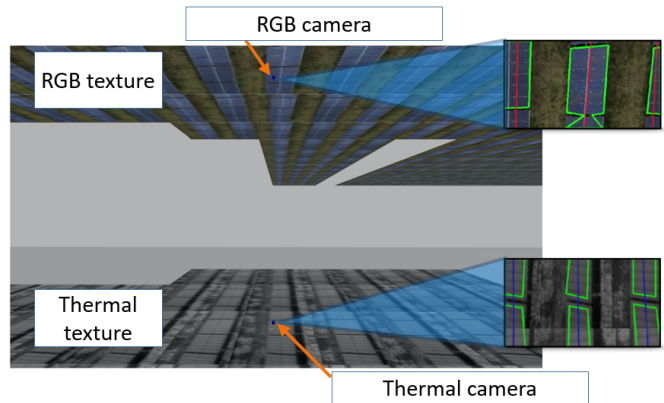


Fig. 6. Gazebo Simulator linked to the Matrice 300 DJI Simulator. Only perception is simulated, by updating the position of the RGB (looking upward) and thermal (looking downward) cameras coherently with the UAV/camera pose returned by the DJI Matrice Simulator.

Gazebo was linked to the UAV position returned by the DJI Matrice Simulator to guarantee coherence in the simulated images returned during the simulated flight. Specifically, RGB textures were placed “above in the sky,” while thermal textures were placed “below on the ground.” By adding two cameras in Gazebo, one directed towards the sky and the other directed towards the ground, we simulated the acquisition of RGB and thermal images of the same PV plant. Textures were produced from images captured by the DJI Zenmuse XT2 during a PV plant inspection in northern Italy, Figure 6.

Both in real-world experiments and in simulation, we initially computed the “reference waypoint path” to be followed by the UAV by considering PV module rows one after the other in boustrophedon mode. Once the start of the first PV row was reached, the optimization process for tuning thresholds depending on environmental conditions was executed by letting the UAV hover at a certain height over the PV module. Then the UAV started moving along the PV module row, using both cameras and the EKF for iteratively correcting the reference path. When the UAV reached *PV end*, the visual tracking stopped, and the UAV moved to the next *PV start*. The mission was considered completed when the UAV had inspected the given number of parallel PV module rows.

The thermal and RGB images were processed, at an approximate frequency of 3 and 5 fps, respectively, both in the simulated and real experiment (computations can be made more efficient to achieve a higher frame rate). Observations are used to correct the estimate of the *PV midline* through the EKF: then, velocity commands for path following are sent to the onboard controller of the DJI Matrice 300 approximately with a 5Hz frequency in simulation (due to heavy computations performed in Gazebo) and a 30Hz frequency in the real case – which, in the following, explains the higher number of control steps in the Figures reporting on real-world experiments.

The following subsections describe results obtained during the simulated and real-world experiments conducted in a PV plant. Simulated experiments (Section VI-B) were mainly aimed to validate the proposed approach and assess the system’s

¹⁰A method to automatically control the UAV altitude depending on the difference between the actual and expected dimensions of PV modules on the image plane was implemented, but it is not discussed in this work.

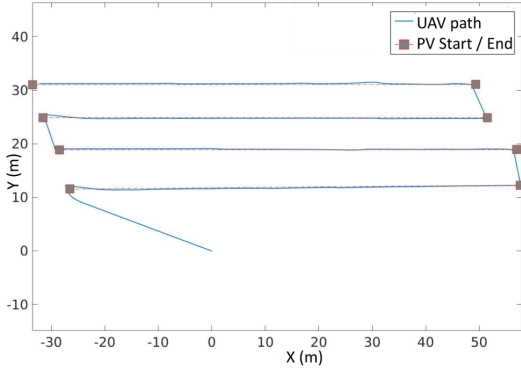
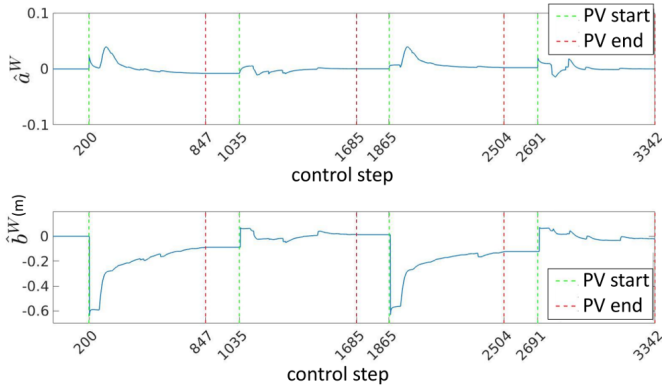


Fig. 7. Projection on the XY-plane of the UAV path (thermal camera).


 Fig. 8. EKF estimation error of the *PV midline* parameters \hat{a}^W and \hat{b}^W (thermal camera).

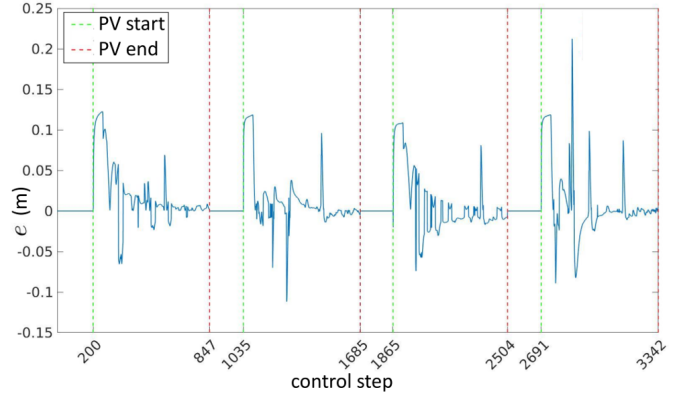
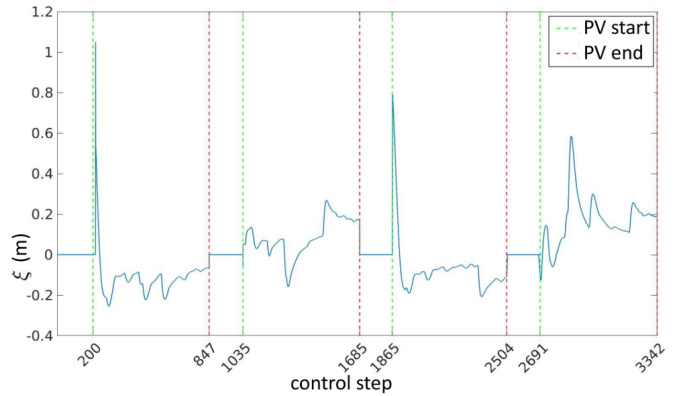
reliability in the presence of inaccurate waypoint positioning. Experiments in the real scenario (Section VI-C) had the primary purpose of comparing the proposed approach's robustness and assessing advantages deriving from combining thermal and RGB cameras.

B. Experimental Results in Simulation

Two classes of experiments were performed in simulation:

- Subsection VI-B1 reports the simulated experiments with the thermal camera only, RGB camera only, and both cameras for PV module detection. Here we do not consider errors in waypoints, which are correctly located on the midlines of the corresponding PV rows.
- Subsection VI-B2 reports the simulated experiments with both cameras to assess the robustness of the approach in the presence of errors in waypoint positioning.

1) *Testing the impact of different cameras for panel detection:* The mission consisted in inspecting four parallel PV rows. The waypoints were assumed to be correctly placed at each row's start and end without errors. During navigation, the UAV velocity had a constant value of 0.6m/s, and the UAV flew at a constant height of 15m from the take-off point. Please notice that, at a 15m height, a speed lower than 2m/s is appropriate to prevent blurred images and ensure image overlapping.


 Fig. 9. Control error e from the estimated *PV midline* (thermal camera).

 Fig. 10. Navigation error ξ from the real *PV midline* (thermal camera).

Experiments were initially performed with the thermal camera only. In Figure 7, the projection on the XY-plane of the path followed by the UAV along four parallel PV rows (blue line) and the reference path determined by the waypoints (red dashed line) are shown. After take-off, the UAV autonomously reached the first *PV start*, and hovered there for some second before moving along the panels, collecting observations to estimate the *PV midline*. Navigation performance can be evaluated by measuring the convergence of the UAV position to the midline of PV module rows.

In Figure 8, the error between the real *PV midline* $m = (a^W, b^W)$ (the ground truth is known in simulation) and the estimated state $\hat{m} = (\hat{a}^W, \hat{b}^W)$ returned by the EKF is shown. Green vertical lines correspond to *PV start*; red vertical lines correspond to *PV end* of the same row. Since the UAV moved from the end of one row to the start of the next one by using positioning information provided by the onboard flight controller, the plots included between a red vertical line and the subsequent green line shall be ignored since they correspond to a change of PV module row.

In Figure 9, the control error e between the UAV position and the *PV midline* estimated with the EKF is shown, with average $\mu_e = 0.022\text{m}$ and standard deviation $\sigma_e = 0.031\text{m}$ (we consider only values included between a green vertical line and the subsequent red vertical line).

In Figure 10, the navigation error ξ between the UAV

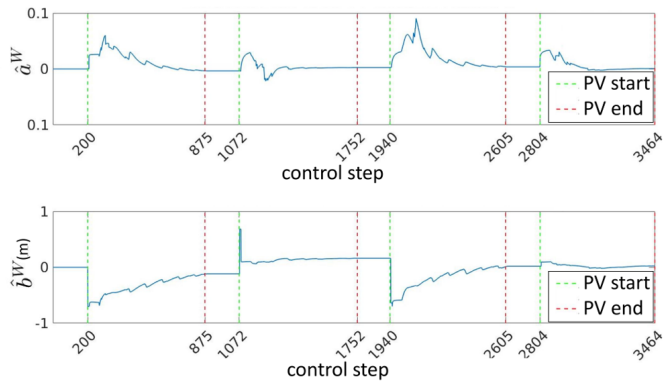


Fig. 11. EKF estimation error of the *PV midline* parameters \hat{a}^W and \hat{b}^W (RGB camera).

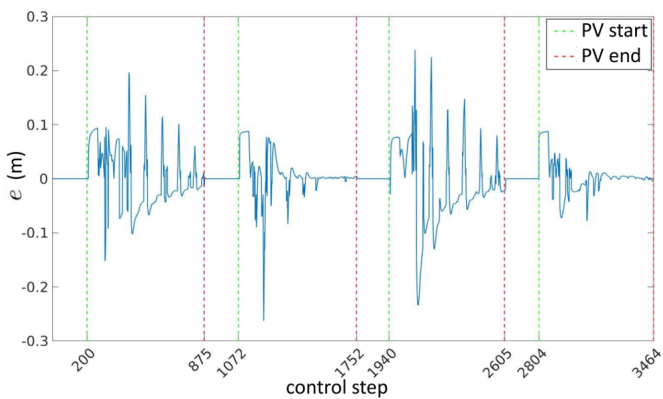


Fig. 12. Control error e from the estimated *PV midline* (RGB camera).

position and the actual *PV midline* (the ground truth is known in simulation) is shown. The navigation error has an average $\mu_\xi = 0.145\text{m}$ and a standard deviation $\sigma_\xi = 0.132\text{m}$. The figure shows that the navigation error tends to be larger when the UAV starts to track the *PV module row* after reaching *PV start*, green vertical line. This is coherent with the fact that *PV start* is considered to be reached when the UAV position is within a 1-meter distance, thus producing an initial error that is recovered later.

Next, experiments were performed with the RGB camera only. The projection on the XY-plane of the UAV path using the RGB camera is not reported since it is difficult to appreciate differences with the previous experiment. Figure 11 reports the error between the actual and the estimated state of the *PV midline*. Figure 12 reports the control error, with average $\mu_e = 0.032\text{m}$ and standard deviation $\sigma_e = 0.036\text{m}$ (i.e., performance is worse than those obtained during the experiment with the thermal camera). Figure 13 reports the navigation error, with average $\mu_\xi = 0.201\text{m}$ and standard deviation $\sigma_\xi = 0.157\text{m}$.

Eventually, experiments were performed with both cameras. Figure 14 reports the error between the actual and the estimated state of the *PV midline*. Figure 15 reports the control error, with average $\mu_e = 0.026\text{m}$ and standard deviation $\sigma_e = 0.036\text{m}$. Figure 16 reports the navigation error, with

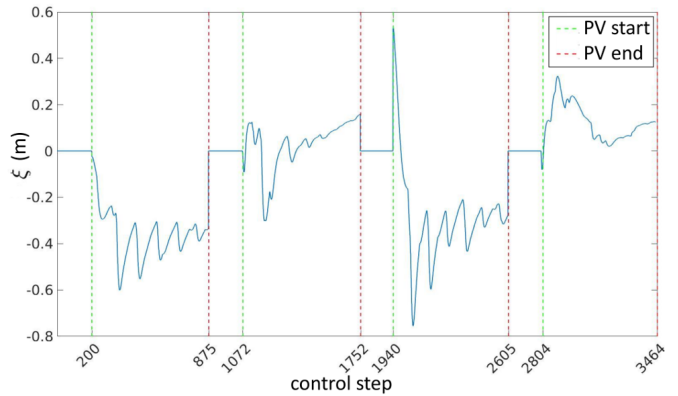


Fig. 13. Navigation error ξ from the real *PV midline* (RGB camera).

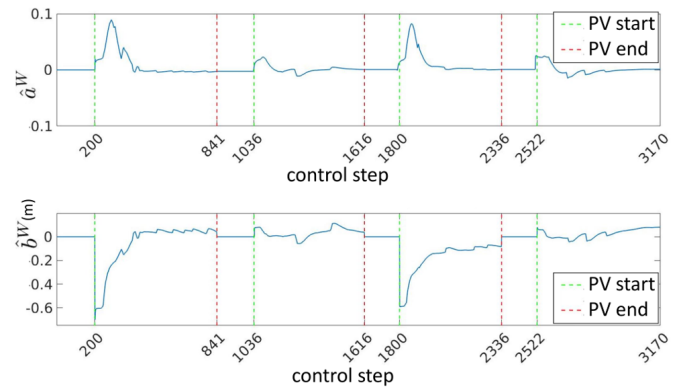


Fig. 14. EKF estimation error of the *PV midline* parameters \hat{a}^W and \hat{b}^W (both cameras).

average $\mu_\xi = 0.137\text{m}$ and standard deviation $\sigma_e = 0.150\text{m}$. As expected, the presence of both thermal and RGB cameras slightly improves navigation performance.

2) *Navigation with errors in waypoint positions*: Tests were performed by considering large errors in the positions of waypoints at the start and at the end of *PV module rows* to simulate inaccurate waypoint positions computed from Google Earth images. An example is shown in Figure 17, with navigation performed using both cameras: waypoints do not correspond to *PV start* and *PV end* of actual *PV module rows* since they are subject to a rototranslation error plus additional noise.

However, observing the actual UAV's path (blue curve in Figure 17) shows that the UAV reached the correct *PV start* on the second, third, and fourth *PV row*, thus compensating for large errors due to waypoint wrong placement. Figure 18 reports errors in the *PV midline* state estimated by the EKF. The control and navigation errors are comparable with those of the previous experiments: the control error in Figure 19 has an average $\mu_e = 0.022\text{m}$ and standard deviation $\sigma_e = 0.033\text{m}$. The navigation error in Figure 20 has average $\mu_\xi = 0.109\text{m}$ and standard deviation $\sigma_e = 0.114\text{m}$.

C. Results in Real-World Experiments

Experiments were conducted in a *PV plant* in Predosa in Northern Italy, exploring different configurations:

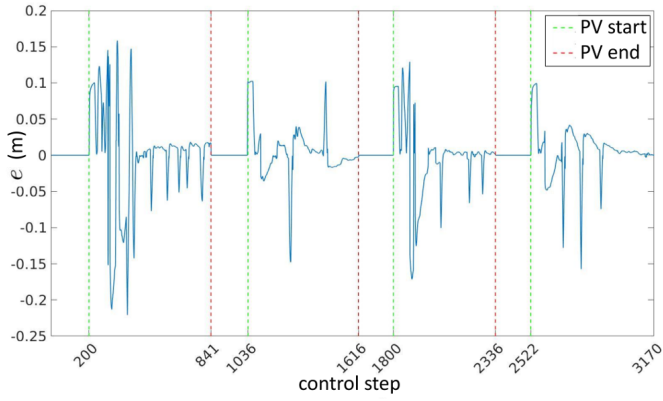


Fig. 15. Control error e from the estimated *PV midline* (both cameras).

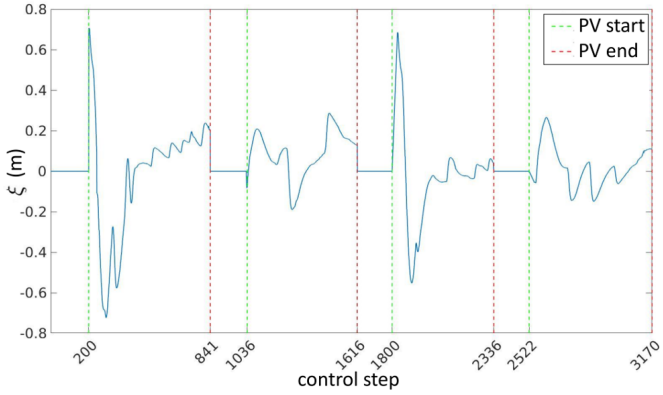


Fig. 16. Navigation error ξ from the real *PV midline* (both cameras).

- Subsection VI-C1 explores navigation along one PV module row using the thermal camera only.
- Subsection VI-C2 explores navigation along one PV module row using the RGB camera only.
- Subsections VI-C3 and VI-C4 explore navigation along one/four PV rows using both thermal and RGB cameras.

In initial tests, the UAV moved at a desired height from the ground of 15m and a desired speed of 1m/s.

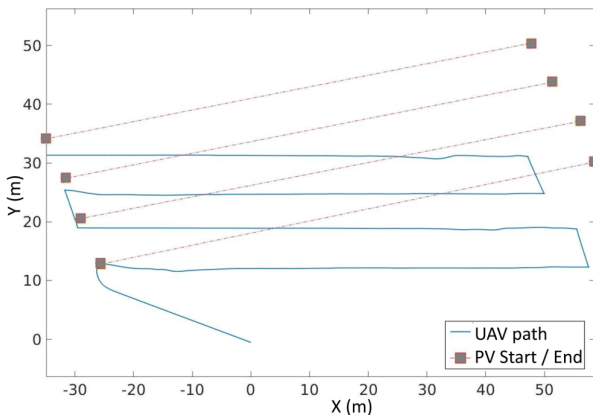


Fig. 17. Projection on the XY-plane of the UAV path in the presence of waypoint positioning errors (both cameras).

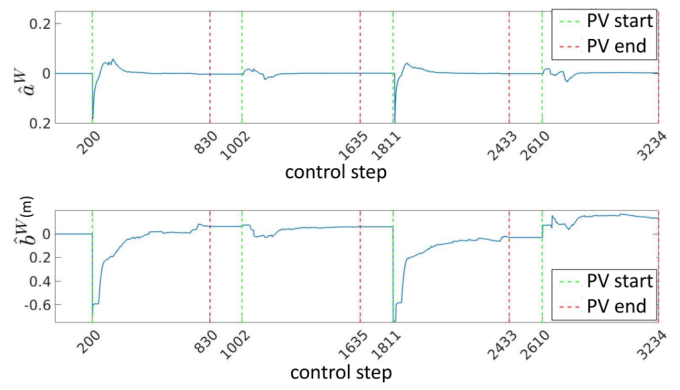


Fig. 18. EKF estimation error of the *PV midline* parameters \hat{a}^W and \hat{b}^W in the presence of waypoint positioning errors (both cameras).

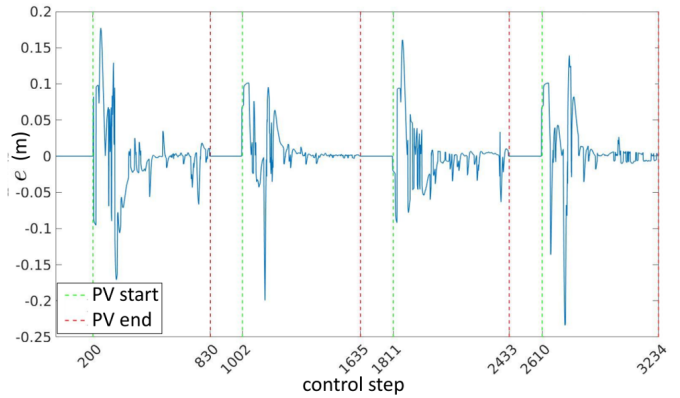


Fig. 19. Control error e from the estimated *PV midline* in the presence of waypoint positioning errors (both cameras).

1) *Navigation with Thermal Camera only:* An example of PV module detection in Predosa, obtained using the thermal camera, is shown in Figure 21 on the left.

In Figure 22, the projection on the XY-plane of the UAV path is shown. After take-off, the UAV was manually guided to the first waypoint: in this phase, the control error e and the navigation error ξ are not computed, which explains why they are constantly zero in Figures 23-31. Next, the UAV started

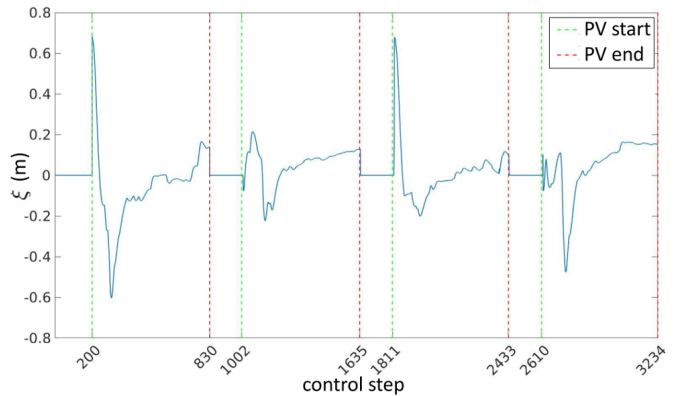


Fig. 20. Navigation error ξ from the real *PV midline* in the presence of waypoint positioning errors (both cameras).

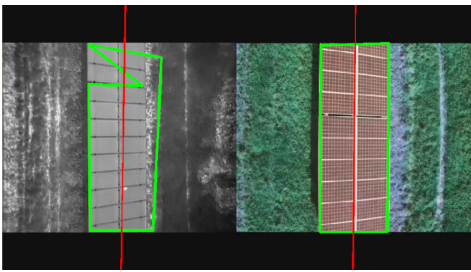


Fig. 21. PV modules detection in Predosa, Italy (15 m from the ground).

collecting observations to estimate the parameters \hat{a}^W and \hat{b}^W of the *PV midline*. Since the UAV does not move until the estimation error is below a given threshold at the *PV start* of each row, the duration of this phase may vary in different experiments or when tracking different PV rows within the same experiment. The average control and navigation errors μ_e and μ_ξ are computed only after the UAV has reached the speed of 1m/s after a transitory (i.e., the sometimes significant errors at the start of PV rows are not considered).

Please also notice that, in real-world experiments, the position of the PV module row in the world and the corresponding *PV start* and *PV end* were estimated before operations using a GPS since the ground truth is known only in simulation. However, this information was not used for path-following: it is only used in the Figures for representation purposes. PV tracking was performed during navigation using the control method described in the previous Sections, and the navigation error ξ was computed by manually inspecting the video stream acquired by onboard cameras (once again because the ground truth is not available in this case). To this end, the video stream was periodically sampled (with a period of about four seconds), and images were manually inspected to measure the distance in pixels and then in meters¹¹ between the center of the image and the center of the PV module row (ξ tends to zero as this distance tends to zero).

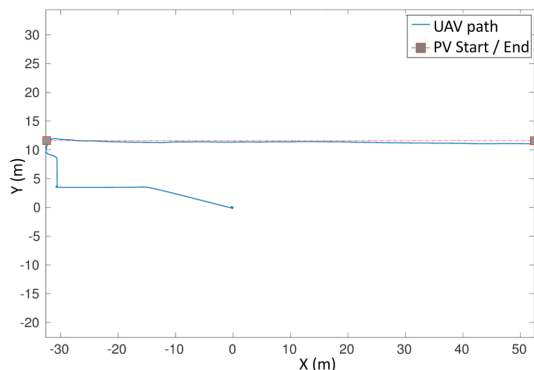


Fig. 22. Projection on the XY-plane of the UAV path (thermal camera).

In Figure 23, the control error e is shown (i.e., the distance from the estimated *PV midline*), with a significant initial error due to inaccurate detection of the *PV midline* (which was

¹¹The meters/pixel ratio is computed by knowing the width in meters of a PV module and measuring its corresponding width in pixels in the image.

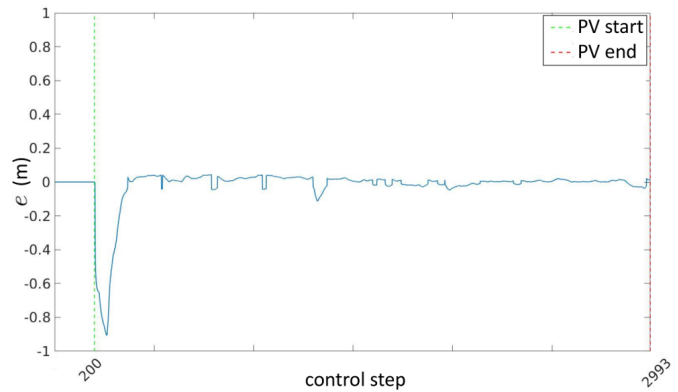


Fig. 23. Control error from the estimated *PV midline* (thermal camera).

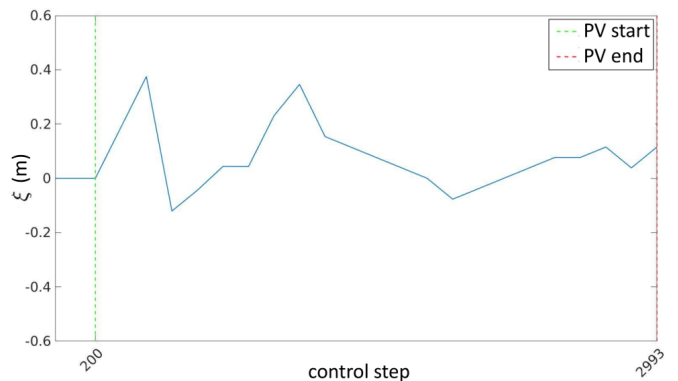


Fig. 24. Navigation error from the real *PV midline* (thermal camera).

later recovered), average $\mu_e = 0.012\text{m}$, and standard deviation $\sigma_e = 0.010\text{m}$. In Figure 24, the navigation error ξ , computed as described before, is shown (i.e., the distance from the actual *PV midline*), with average $\mu_\xi = 0.056\text{m}$ and standard deviation $\sigma_\xi = 0.040\text{m}$.

2) *Navigation with RGB Camera only*: An example of PV module detection using the RGB camera only is shown in Figure 21 on the right.

The projection on the XY-plane of the UAV path is not reported since it would be difficult to appreciate differences with the previous test. In Figure 25, the control error e is shown, with average $\mu_e = 0.023\text{m}$ and standard deviation $\sigma_e = 0.019\text{m}$. In Figure 26, the navigation error ξ is shown, with average $\mu_\xi = 0.083\text{m}$ and standard deviation $\sigma_\xi = 0.074\text{m}$.

3) *Navigation with both cameras*: The same test was performed with the thermal and RGB cameras for *PV midline* estimation and navigation. Once again, the UAV path is not reported since it would be challenging to appreciate differences from the previous tests.

In Figure 27, the control error e is shown, with $\mu_e = 0.010\text{m}$ and $\sigma_e = 0.008\text{m}$. In Figure 28, the navigation error ξ is shown, with $\mu_\xi = 0.046\text{m}$ and $\sigma_\xi = 0.027\text{m}$. The average navigation error is lower than the one of the previous cases, as also visible in the Figure.

4) *Navigation with both cameras along 4 rows*: Additional experiments were performed, using both cameras, along 4

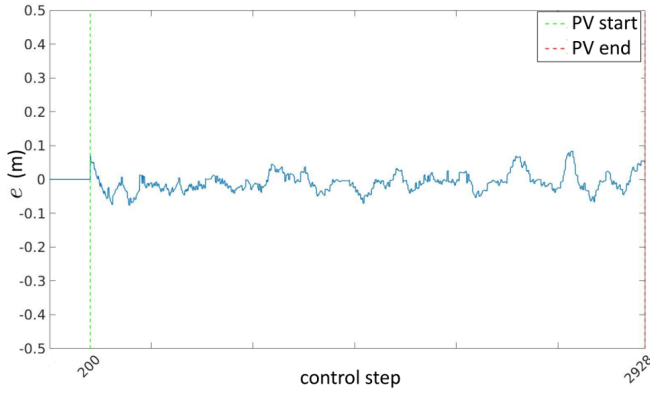


Fig. 25. Control error from the estimated *PV midline* (RGB camera).

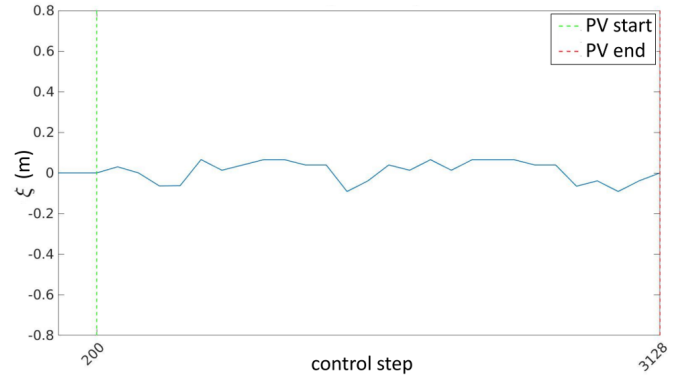


Fig. 28. Navigation error from the real *PV midline* (both cameras).

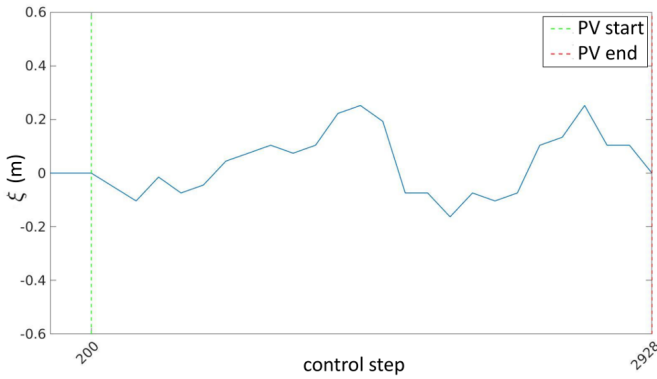


Fig. 26. Navigation error from the real *PV midline* (RGB camera).

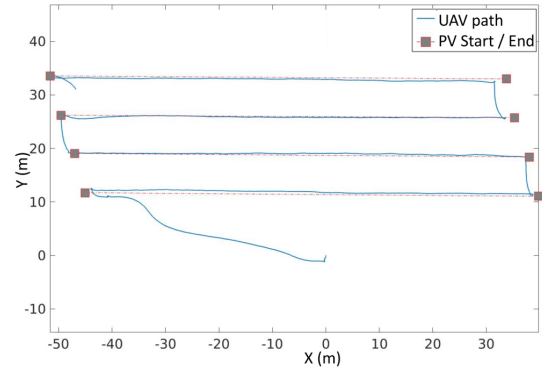


Fig. 29. Projection on the XY-plane of the UAV path (both cameras).

longer path involving four rows, to confirm the capability of the system to autonomously inspect PV plants. Figure 29 reports the UAV path corresponding to one of these experiments with a higher speed of 1.2m/s.

Figure 30 reports the control error: the error in the first, second, third and fourth PV rows has, respectively, average and standard deviation $\mu_e = 0.021\text{m}$, $\sigma_e = 0.020\text{m}$; $\mu_e = 0.019\text{m}$, $\sigma_e = 0.013\text{m}$; $\mu_e = 0.020\text{m}$, $\sigma_e = 0.015\text{m}$; $\mu_e = 0.042\text{m}$, $\sigma_e = 0.024\text{m}$. Figure 31 reports the navigation error, with $\mu_\xi = 0.141\text{m}$, $\sigma_\xi = 0.095\text{m}$; $\mu_\xi = 0.165\text{m}$, $\sigma_\xi = 0.108\text{m}$;

$\mu_\xi = 0.123\text{m}$, $\sigma_\xi = 0.093\text{m}$; $\mu_\xi = 0.087\text{m}$, $\sigma_\xi = 0.037\text{m}$. It can be observed that higher navigation errors can sometime occur, especially after moving from a row to the subsequent one using the embedded positioning system (based on GPS, IMUs and compass); however, such error is bounded and the system is able to recover from it.

VII. CONCLUSION

This article presented a new approach for autonomous UAV inspection of a PV plant based on the detection and tracking of PV modules through thermal and RGB cameras, which

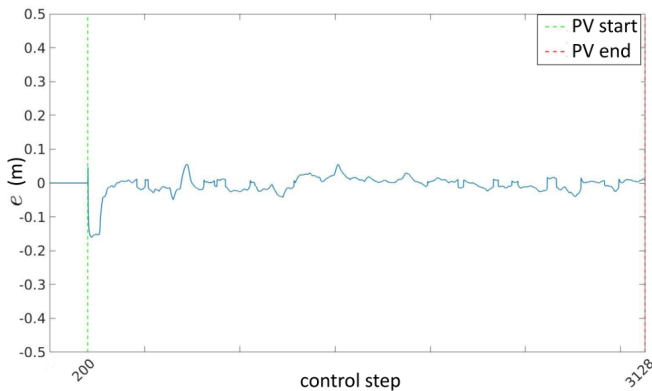


Fig. 27. Control error from the estimated *PV midline* (both cameras)

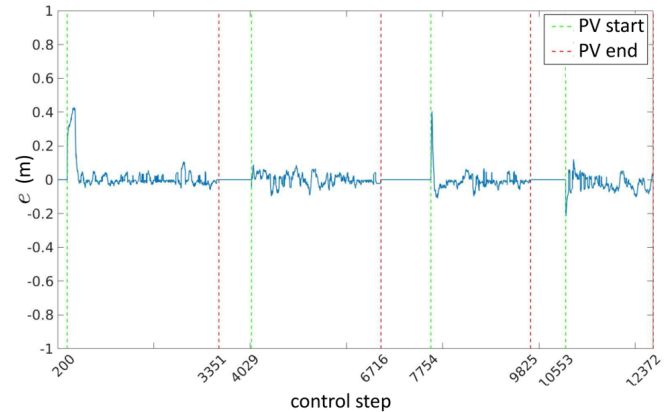


Fig. 30. Control error from the estimated *PV midline* (both cameras).

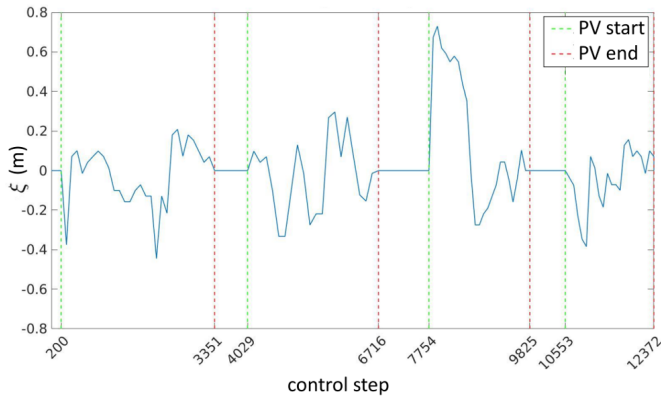


Fig. 31. Navigation error from the real *PV midline* (both cameras).

is an alternative to traditional approaches based on UAV photogrammetry. The proposed approach is based on:

- A procedure for detecting PV modules in real-time using a thermal or an RGB camera (or both).
- A procedure to correct errors in the relative position of the *PV midline*, initially estimated through GPS, by merging thermal and RGB data.
- A navigation system provided with a sequence of georeferenced waypoints defining an inspection path over the PV plant, which uses the estimated position of the *PV midline* to make the UAV move along the path with bounded navigation errors.

The system was tested both in a simulated and in a real PV plant with a DJI Matrice 300. Results suggest that the solution proposed meets the constraints for autonomous PV inspection. Indeed, it produces navigation errors that are sufficiently small to keep the PV modules within the camera field of view when flying at a 15m height, which allows for acquiring overlapping high-resolution thermal images for defect detection. Most importantly, navigation errors are small in the presence of errors in waypoint positions. Georeferenced waypoints computed from Google Earth images and GPS data may be affected by large biases but tend to be locally coherent. Results confirm that alternating (i) visual servoing along a PV row with (ii) GPS-based navigation when moving from one row to the subsequent one turns out to be a feasible solution.

Tests confirmed that combining both cameras tends to reduce average errors. Additionally, we conjecture that using two sensors based on completely different principles for PV module segmentation can make the whole process more reliable when thermal or lighting conditions are suboptimal. For example, when the PV panel heat may not be clearly distinguishable from the surrounding environment (e.g., early in the morning, especially in winter) or when the sun glares can negatively affect color-based segmentation.

We will explore planning procedures to automatically extract a sequence of georeferenced waypoints from Google Earth images in future work. This task is far from being straightforward since the PV plant might have an irregular shape, be built on non-flat terrain, and be traversed by roads or power line infrastructures. Indeed, PV module rows are not

necessarily arranged in the best way to be covered following a boustrophedon path. Eventually, even if we argue that a model-based approach may offer many advantages in the considered scenario, we plan to evaluate Machine Learning techniques for PV module segmentation. This will enable fairer comparisons between model- and data-driven approaches in autonomous, UAV-based inspection of PV plants.

REFERENCES

- [1] R. Heinberg and D. Fridley, *Our Renewable Future: Laying the Path for One Hundred Percent Clean Energy*. Island Press, 2016.
- [2] “Eurostat: Renewable energy statistics.” [Online]. Available: https://ec.europa.eu/eurostat/statistics-explained/index.php?title=Renewable_energy_statistics
- [3] G. Petrone, G. Spagnuolo, R. Teodorescu, M. Veerachary, and M. Vitelli, “Reliability issues in photovoltaic power processing systems,” *IEEE T. Ind. Electron.*, vol. 55, no. 7, pp. 2569–2580, 2008.
- [4] F. Grimaccia, S. Leva, A. Dolara, and M. Aghaei, “Survey on PV Modules Common Faults After OM Flight Extensive Campaign Over Different Plants in Italy,” *IEEE J. Photovolt.*, vol. 7, no. 3, pp. 810–816, 2017.
- [5] J. A. Tsanakas, L. Ha, and C. Buerhop, “Faults and infrared thermographic diagnosis in operating c-si photovoltaic modules: A review of research and future challenges,” *Renew. Sust. Energ. Rev.*, vol. 62, pp. 695–709, 2016.
- [6] P. B. Quater, F. Grimaccia, S. Leva, M. Mussetta, and M. Aghaei, “Light Unmanned Aerial Vehicles (UAVs) for Cooperative Inspection of PV Plants,” *IEEE J. Photovolt.*, vol. 4, no. 4, pp. 1107–1113, 2014.
- [7] V. Carletti, A. Greco, A. Saggese, and M. Vento, “Multi-object tracking by flying cameras based on a forward-backward interaction,” *IEEE Access*, vol. 6, pp. 43905–43919, 2018.
- [8] S. Djordjevic, D. Parlevliet, and P. Jennings, “Detectable faults on recently installed solar modules in western australia,” *Renew. Energy*, vol. 67, pp. 215–221, 2014.
- [9] G. Roggi, A. Niccolai, F. Grimaccia, and M. Lovera, “A computer vision line-tracking algorithm for automatic uav photovoltaic plants monitoring applications,” *Energies*, vol. 13, no. 4, 2020.
- [10] S. Hartmut, H. Dirk, S. Blumenthal, T. Linder, P. Molitor, and V. Tretyakov, “Teleoperated visual inspection and surveillance with unmanned ground and aerial vehicles,” *Int. J. Online Biomed. Eng.*, vol. 13, pp. 26–38, 2020.
- [11] S. Rathinam, Z. Kim, A. Soghikian, and R. Sengupta, “Vision based following of locally linear structures using an unmanned aerial vehicle,” in *CDC’05*, 2005, pp. 6085–6090.
- [12] E. Honkavaara, H. Saari, J. Kaivosoja, I. Pölonen, T. Hakala, P. Litkey, J. Mäkyinen, and L. Pesonen, “Processing and assessment of spectrometric, stereoscopic imagery collected using a lightweight uav spectral camera for precision agriculture,” *Remote Sens.*, vol. 5, no. 10, pp. 5006–5039, 2013.
- [13] N. Metni and T. Hamel, “A uav for bridge inspection: Visual servoing control law with orientation limits,” *Autom. Constr.*, vol. 17, no. 1, pp. 3–10, 2007.
- [14] M. Aghaei, A. Dolara, S. Leva, and F. Grimaccia, “Image resolution and defects detection in PV inspection by unmanned technologies,” in *PESGM 2016*, 2016, pp. 1–5.
- [15] Y. Zefri, A. Elkettani, I. Sebari, and S. Lamallam, “Thermal infrared and visual inspection of photovoltaic installations by uav photogrammetry—application case: Morocco,” *Drones*, vol. 2, no. 4, pp. 1–24, 2018.
- [16] Y. Zefri, I. Sebari, H. Hajji, and G. Aniba, “Developing a deep learning-based layer-3 solution for thermal infrared large-scale photovoltaic module inspection from orthorectified big UAV imagery data,” *Int. J. Appl. Earth Obs. Geoinf.*, vol. 106, 2022.
- [17] S. A. Hassan, S. H. Han, and S. Y. Shin, “Real-time road cracks detection based on improved deep convolutional neural network,” in *CCECE 2020*, 2020, pp. 1–4.
- [18] Y. Pan, X. Zhang, G. Cervone, and L. Yang, “Detection of asphalt pavement potholes and cracks based on the unmanned aerial vehicle multispectral imagery,” *IEEE J. Sel. Top. Appl. Earth Obs. Remote Sens.*, vol. 11, no. 10, pp. 3701–3712, 2018.
- [19] F. Zhang, Y. Fan, T. Cai, W. Liu, Z. Hu, N. Wang, and M. Wu, “OTL-Classifier: Towards imaging processing for future unmanned overhead transmission line maintenance,” *Electronics*, vol. 8, no. 11, 2019.

- [20] A. Zormpas, K. Moirogiorgou, K. Kalaitzakis, G. A. Plokamakis, P. Partsinelos, G. Giakos, and M. Zervakis, "Power transmission lines inspection using properly equipped unmanned aerial vehicle (uav)," in *IST'18*, 2018, pp. 1–5.
- [21] S. Ren, K. He, R. Girshick, and J. Sun, "Faster R-CNN: Towards Real-Time Object Detection with Region Proposal Networks," in *NIPS'15*, 2016.
- [22] R. Duda and P. Hart, "Use of the hough transformation to detect lines and curves in pictures," *Commun. ACM*, vol. 15, no. 1, pp. 11–15, 1972.
- [23] J. A. Tsanakas, L. D. Ha, and F. Al Shakarchi, "Advanced inspection of photovoltaic installations by aerial triangulation and terrestrial georeferencing of thermal/visual imagery," *Renew. Energy*, vol. 102, pp. 224–233, 2017.
- [24] X. Li, Q. Yang, Z. Lou, and W. Yan, "Deep learning based module defect analysis for large-scale photovoltaic farms," *IEEE Trans. Energy Convers.*, vol. 34, no. 1, 2019.
- [25] A. Huerta Herraiz, A. Pliego Marug' an, and F. P. García Márquez, "Photovoltaic plant condition monitoring using thermal images analysis by convolutional neural network-based structure," *Renew. Energy*, vol. 153, pp. 334–348, 2020.
- [26] A. S. Vincenzo Carletti, Antonio Greco and M. Vento, "An intelligent flying system for automatic detection of faults in photovoltaic plants," *J. Ambient Intell. Humaniz. Comput.*, vol. 11, pp. 2027–2040, 2020.
- [27] A. Fernández, R. Usamentiaga, P. de Arquer, M. Fernández, D. Fernández, J. Carús, and M. Fernández, "Robust detection, classification and localization of defects in large photovoltaic plants based on unmanned aerial vehicles and infrared thermography," *Appl. Sci.*, vol. 10, no. 17, 2020.
- [28] Y. Zefri, A. Elkcttani, I. Sebari, and S. A. Lamallam, "Inspection of photovoltaic installations by thermo-visual uav imagery application case: Morocco," in *IRSEC 2017*, 2017, pp. 1–6.
- [29] I. Souffer, M. Sghiouar, I. Sebari, Y. Zefri, H. Hajji, and G. Aniba, "Automatic extraction of photovoltaic panels from uav imagery with object-based image analysis and machine learning," *Lect. Notes Electr. Eng.*, vol. 745, pp. 699–709, 2022.
- [30] T. Solend, H. Jonas Fossum Moen, and A. Rodningsby, "Modelling the impact of uav navigation errors on infrared pv inspection data quality and efficiency," in *PVSC'21*, 2021, pp. 991–996.
- [31] A. M. Moradi Sizkouhi, S. Majid Esmailifar, M. Aghaei, A. K. Vidal de Oliveira, and R. Rüter, "Autonomous Path Planning by Unmanned Aerial Vehicle (UAV) for Precise Monitoring of Large-Scale PV plants," in *PVSC'19*, 2019.
- [32] A. M. Moradi Sizkouhi, M. Aghaei, S. M. Esmailifar, M. R. Mohammadi, and F. Grimaccia, "Automatic boundary extraction of large-scale photovoltaic plants using a fully convolutional network on aerial imagery," *IEEE J. Photovol.*, vol. 10, no. 4, pp. 1061–1067, 2020.
- [33] A. M. Moradi Sizkouhi, M. Aghaei, and S. M. Esmailifar, "Aerial Imagery of PV Plants for boundary detection," 2020. [Online]. Available: <https://iee-dataport.org/documents/aerial-imagery-pv-plants-boundary-detection>
- [34] S. Rathinam, Z. Kim, A. Soghikian, and R. Sengupta, "Vision based following of locally linear structures using an unmanned aerial vehicle," in *CDC'05*, 2005, pp. 6085–6090.
- [35] R. Raguram, J.-M. Frahm, and M. Pollefeys, "A comparative analysis of ransac techniques leading to adaptive real-time random sample consensus," in *ECCV'08*, D. Forsyth, P. Torr, and A. Zisserman, Eds. Berlin, Heidelberg: Springer Berlin Heidelberg, 2008, pp. 500–513.
- [36] A. Majeed, M. Abbas, F. Qayyum, K. T. Miura, M. Y. Misro, and T. Nazir, "Geometric modeling using new cubic trigonometric b-spline functions with shape parameter," *Mathematics*, vol. 8, no. 12, 2020.
- [37] J. A. Sarapura, F. Roberti, R. Carelli, and J. M. Sebastián, "Passivity based visual servoing of a uav for tracking crop lines," in *RPIC'17*, 2017, pp. 1–6.
- [38] G.-Y. Li, R.-T. Soong, J.-S. Liu, and Y.-T. Huang, "Uav system integration of real-time sensing and flight task control for autonomous building inspection task," 2019.
- [39] L.-C. Chen, Y. Zhu, G. Papandreou, F. Schroff, and H. Adam, "Encoder-decoder with atrous separable convolution for semantic image segmentation," in *ECCV'18*, 2018.
- [40] G. Roggi, A. Niccolai, F. Grimaccia, and M. Lovera, "A computer vision line-tracking algorithm for automatic UAV photovoltaic plants monitoring applications," *Energies*, vol. 13, no. 4, 2020.
- [41] Z. Xi, Z. Lou, Y. Sun, X. Li, Q. Yang, and W. Yan, "A vision-based inspection strategy for large-scale photovoltaic farms using an autonomous UAV," in *DCABES'18*, 2018, pp. 200–203.
- [42] A. Barredo Arrieta, N. Díaz-Rodríguez, J. Del Ser, A. Bennetot, S. Tabik, A. Barbado, S. García, S. Gil-Lopez, D. Molina, R. Benjamins, R. Chatila, and F. Herrera, "Explainable explainable artificial intelligence (XAI): Concepts, taxonomies, opportunities and challenges toward responsible ai," *Inf. Fusion*, vol. 58, 2020.
- [43] S. Thys, W. Ranst, and T. Goedeme, "Fooling automated surveillance cameras: Adversarial patches to attack person detection," in *CVPR'19*, vol. 2019-June, 2019.
- [44] A. Haponik, "Fly to the sky! With AI. How is artificial intelligence used in aviation?" [Online]. Available: <https://addepto.com/fly-to-the-sky-with-ai-how-is-artificial-intelligence-used-in-aviation/>
- [45] S. Schirmer, C. Torens, F. Nikodem, and J. Dauer, "Considerations of artificial intelligence safety engineering for unmanned aircraft," in *SAFECOMP'18*, B. Gallina, A. Skavhaug, E. Schoitsch, and F. Bitsch, Eds. Cham: Springer International Publishing, 2018, pp. 465–472.
- [46] Stanford Artificial Intelligence Laboratory et al., "Robotic operating system." [Online]. Available: <https://www.ros.org>
- [47] C. Zhu, R. Byrd, P. Lu, and J. Nocedal, "Algorithm 778: L-bfgs-b: Fortran subroutines for large-scale bound-constrained optimization," *ACM Trans. Math. Softw.*, vol. 23, no. 4, pp. 550–560, 1997.
- [48] F. E. Daum, *Extended Kalman Filters*. London: Springer London, 2015, pp. 411–413.
- [49] F. Capezio, A. Sgorbissa, and R. Zaccaria, "GPS-based localization for a surveillance UGV in outdoor areas," vol. 2005, 2005, pp. 157–162.
- [50] A. Sgorbissa, "Integrated robot planning, path following, and obstacle avoidance in two and three dimensions: Wheeled robots, underwater vehicles, and multicopters," *Int. J. Rob. Res.*, vol. 38, no. 7, pp. 853–876, 2019.